Astroparticle Physics 146 (2023) 102793

Contents lists available at ScienceDirect

Astroparticle Physics

journal homepage: www.elsevier.com/locate/astropartphys

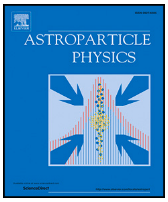

Thermal neutron background at Laboratorio Subterráneo de Canfranc (LSC)

J. Plaza [a,*], T. Martínez [a], V. Bécares [a], D. Cano-Ott [a], D. Villamarín [a], A. Pérez de Rada [a], E. Mendoza [a], V. Pesudo [a], R. Santorelli [a], C. Peña [b], J. Balibrea-Correa [c,d,f], A. Boeltzig [c,e,g]

[a] *Centro de Investigaciones Energéticas, Medioambientales y Tecnológicas (CIEMAT), Avenida Complutense 40, 28040 Madrid, Spain*
[b] *Laboratorio Subterráneo de Canfranc (LSC), Paseo de los Ayerbe s/n, 22880, Canfranc-Estación, Spain*
[c] *Universitá degli Studi di Napoli "Federico I", Italy*
[d] *INFN, Sezione di Napoli, 80126 Napoli, Italy*
[e] *INFN, Laboratorio Nazionale del Gran Sasso, Via G. Acitelli 22, 6711 Asergi, Italy*
[f] *Instituto de Física Corpuscular, CSIC-Universidad de Valencia, 46071 Valencia, Spain*[1]
[g] *Helmholtz-Zentrum Dresden-Rossendorf (HZDR), Bautzner Landstraße 400, 01328 Dresden*[2]

ARTICLE INFO

Keywords:
Underground neutron background
Thermal neutron flux
^{3}He proportional counter
Pulse shape discrimination

ABSTRACT

The thermal neutron background at Laboratorio Subterráneo de Canfranc (LSC) has been determined using several ^{3}He proportional counter detectors. Bare and Cd shielded counters were used in a series of long measurements. Pulse shape discrimination techniques were applied to discriminate between neutron and gamma signals as well as other intrinsic contributions. Montecarlo simulations allowed us to estimate the sensitivity of the detectors and calculate values for the background flux of thermal neutrons inside Hall-A of LSC. The obtained value is $(3.5\pm0.8)\times10^{-6}$ n/cm^{2}s, and is within an order of magnitude compared to similar facilities.

1. Introduction

Underground laboratories are unique facilities for the study of rare events phenomena. The rock overburden of such facilities attenuates the cosmic rays and their secondary by-products, like gamma rays, electrons and neutrons, by several orders of magnitude, resulting in a low background environment.

Experiments in the field of rare event search (e.g. neutrinoless double beta decay, direct dark matter detection) or in the measurement of cross sections of astrophysical reactions, require the best possible characterization of this background. Particularly, the measurement of the neutron flux in an underground laboratory, both the integral value and the energy distribution, is essential for this type of physics. While fast neutrons can produce elastic or inelastic scattering, low-energy neutrons (below 1 keV) can undergo a capture reaction in the structural elements of the detector, and gamma rays produced in the de-excitation of the nucleus can give an important contribution to the background of experiments.

Several measurements of the fast neutron flux have been carried out in different underground laboratories during the recent years [1–4]. In comparison the thermal or epithermal neutron flux is typically less well known and few or no experimental measurements are available for some facilities. This is the case of Laboratorio Subterráneo de Canfranc (LSC). At LSC, where research activities in neutrino-less double beta decay and dark matter fields are carried out since the 90's, only two neutron flux determination measurements have been reported until now. In a first work focused in dark matter search with Germanium detectors, Carmona et al. [1] reported an integral neutron flux of $\Phi_{\mathrm{LAB2500}} = (3.82 \pm 0.44) \times 10^{-6}\mathrm{cm}^{-2}\mathrm{s}^{-1}$ for neutron energies greater than 5 keV in LAB2500 of LSC. The study of the detector response with different shielding setups allowed them to estimate the fast neutron flux. No attempt to estimate the thermal neutron flux was made.

In a second work, Jordan et al. [2,3] made use of several ^{3}He detectors with polyethylene shieldings of different thickness with the specific aim to measure the neutron flux in Hall-A of LSC. They obtained the neutron flux distribution as a function of energy in a range up to 10 MeV. A final integral value of $\Phi_{\mathrm{HallA}} = 1.38 \times 10^{-5}\mathrm{cm}^{-2}\mathrm{s}^{-1}$ was obtained. The setup had a limited sensitivity at thermal energies, yielding values between 0.02 to $2.2 \times 10^{-6}\mathrm{cm}^{-2}\mathrm{s}^{-1}$ for the energy range E<0.5 eV, depending on the method used in the unfolding.

In this paper we present the results of a dedicated measurement of the thermal neutron flux at the center of Hall-A, performed using several ^{3}He detectors. It is the first measurement specifically aimed to

---

* Corresponding author.
E-mail address: julio.plaza@ciemat.es (J. Plaza).

[1] Current Affiliation.

[2] Current Affiliation.

https://doi.org/10.1016/j.astropartphys.2022.102793
Received 11 January 2022; Received in revised form 21 October 2022; Accepted 8 November 2022
Available online 12 November 2022

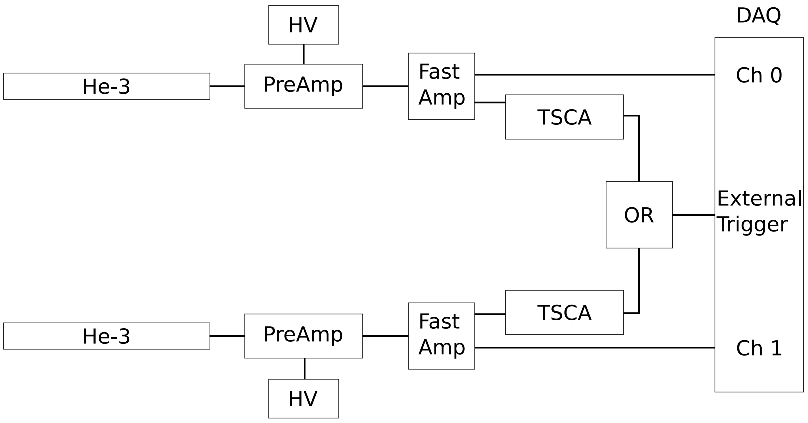

Fig. 1. Scheme of the electronic chain from detector to DAQ. For clarity, only two detectors are shown.

Table 1
Specifications of the ^{3}He detectors from LND Inc. used in this work.

Model	25241	252266
Cathode Material	Aluminum	Stainless Steel
Cathode thickness (mm)	0.89	0.51
Active diameter (mm)	23.62	24.38
Active length (mm)	500.1	600
Partial pressure (torr)	3762 (^{3}He) 3762 (Ar)	7524 (^{3}He) –
Quenching gas (torr)	76 (CO_2)	76 (CO_2)

obtain the neutron flux at thermal energies at LSC and it constitutes a first phase in the design of a continuous monitor of neutron flux.

2. Experimental setup

The measurement was performed with a set of four cylindrical ^{3}He proportional counters of two different models manufactured by LND Inc. [5]. The first two detectors correspond to model 24251, with a cathode made of aluminum and filled with a mixture of gases of ^{3}He, Ar, and CO_2 as quenching gas at a pressure of 10 atm. This model is a Position Sensitive Detector with two outputs, one at each end, but only one was used for these measurements.

The other detectors were model 252266, which includes a cathode made of stainless steel. The filling gas consists of ^{3}He at a pressure of 9.9 atm and CO_2 at a partial pressure of 0.1 atm. Some other detector specifications are listed in Table 1.

The detectors were biased through a charge sensitive preamplifier (Canberra 2006 model). The tube models 24251 and 252266 were operated at 1300 and 1400 V respectively. The amplitude of the preamplified signals were around 14 and 20 mV for the neutron thermal peak, thus the output signals were fed to a fast amplifier CAEN N979B, in order to match the digitizer input range. This fast amplifier preserves the shape and noise/signal ratio of the preamplifier. Finally, the amplified signals were recorded at 100 MS/s and 14 bits resolution using an ADQ14DC-4C-VG 4-channel digitizer from SP Devices [6]. The digitized signals were then processed with dedicated pulse shape algorithms to be described in Section 3.

A second output of the fast amplifier fed an AMP/TSCA ORTEC 590 A module that provided a logic signal when a threshold was exceeded by the amplified signal. This signal was used to generate a common trigger based on a logic OR signal from all detectors. This trigger allowed obtaining a threshold as low as 2 mV in the measurements. The acquisition window extended over 45 μs for each pulse. A sketch of the electronic chain is depicted in Fig. 1.

2.1. Background measurements

The background measurements were carried out in several campaigns since May 2019 until May 2021. The detectors were placed at about 2 m height above ground floor and arranged in the following configurations at different moments of each campaign:

- bare detectors to measure the thermal neutron background,
- detectors wrapped with a cadmium layer of 1 mm thickness to take into account the epithermal background component,
- bare detector inside a polyethylene rectangular prism of 80 cm *x* 80 cm *x* 120 cm dimensions (with almost 40 cm wall thickness) to take into account the intrinsic alpha contamination.

The count rate has been continuously monitored in order to control the stability of the system during the long measurement campaigns and to promptly identify any possible issue induced by the external noise (e.g. vacuum pumps from other surrounding experiments.).

During the measurements, several runs with a 4.8 kBq ^{252}Cf source inside a 1.4 cm thick polyethylene container were also taken for energy calibration and to verify the accuracy of the Monte Carlo simulation. The pulse height spectra of the detectors was clearly different for both detector models as can be seen in Fig. 2 — top, with a much cleaner spectrum for steel cathode detectors due to a lower sensitivity to gamma rays and lower intrinsic alpha contamination.

Visual separation of the neutron and gamma regions can be clearly appreciated for steel detectors, whereas for aluminum detectors the gamma region overlaps with the neutron region below 500 keV. The difference in the partial pressures of ^{3}He between both detector models makes the steel detectors more efficient than the aluminum detectors for neutrons. On the other hand, the combination of He with Ar in the aluminum detectors, results in a higher mass density and thus a higher gamma sensitivity. The wider shape of the neutron peak in the aluminum detector is related to charge collection issues due to the use of only one end of the detector.

The differences are more remarkable when comparing the background measurement, when no sources are present (Fig. 2 — bottom). In low counting rate experiments, alpha and beta particles emitted in the decay of U/Th elements present at the level of ppm in the cathode material becomes an undesirable intrinsic contamination ranging from zero to several MeV. The alpha contamination is larger in detectors made with aluminum cathodes than in those with stainless steel, the difference being greater than one order of magnitude in our case. In addition, the presence of micro-discharges due to bias voltage breakdown in the counter becomes also evident when low rate measurements are carried out as it has also been reported elsewhere [7]. These intrinsic contamination sources are more than enough to nearly hide the neutron component of the spectrum in the aluminum detectors, while allowing

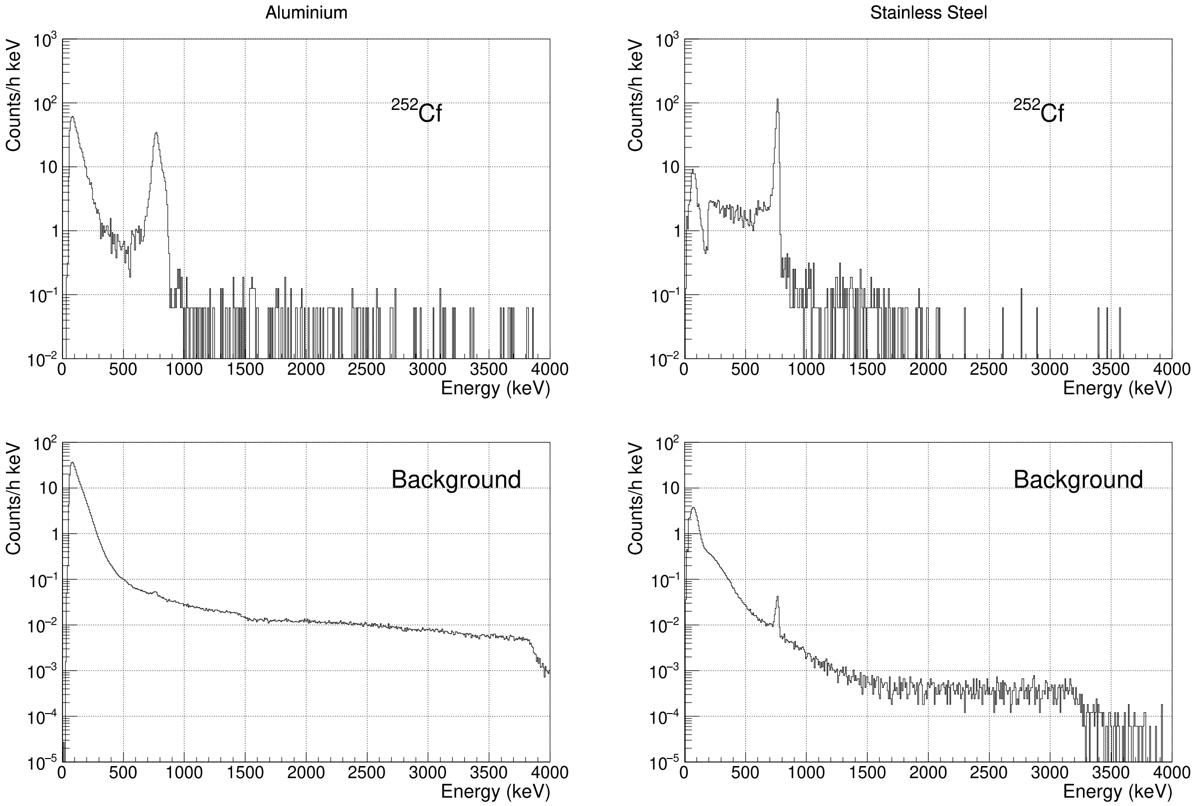

Fig. 2. Pulse height spectra for both type of detectors with a moderated ^{252}Cf source showing the full absorption peak at 764 keV (top) and when only background is measured (bottom).

to show only the total absorption peak in the stainless steel. For this reason, a pulse shape and discrimination analysis approach was applied with the aim to accurately determine the neutron count rates while minimizing the uncertainties.

3. Data analysis

Digitized signals have been analyzed with a dedicated pulse shape routine. A low pass filter (RC = 50 ns) was applied to the signals to remove the high-frequency noise. Pulse parameters have been determined from the smoothed waveform, including baseline, amplitude, time, rise-time, and Root Mean Square (RMS).

According to these parameters, several types of signals have been observed in the collected data. An averaged signal shape for each type of event has been generated and are shown in Fig. 3. Differences in the shape allow to discriminate between types of events.

3.1. Event discrimination

The best discrimination has been obtained using the rise-time between 10 and 50% of the amplitude, and the RMS in the tail region of the signals. It can be shown that for an exponential with decay time τ and initial amplitude A_0, the RMS is related to τ as:

$$RMS \propto A_0\sqrt{\tau} \tag{1}$$

The RMS of the pulse tail normalized to the amplitude is smaller for those signals with shorter decay times as is the case of micro-discharges. Due to the long range taken for the calculation of the RMS (27 μs), a very clean separation can be achieved for micro-discharges.

On the other hand, the rise-time also allows to identify the different types of events [8]: micro-discharge signals have the fastest rise-time, γ/β signals show larger rise-times and low deposited energy, and neutron/α events have intermediate rise-times.

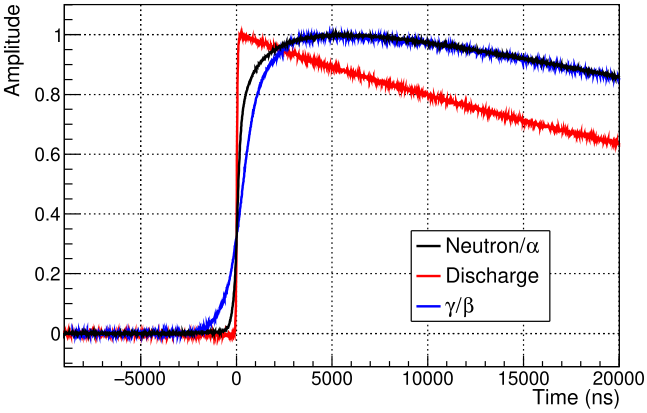

Fig. 3. Averaged signal shapes of different types of events observed in the proportional counters.

Micro-discharges are more effectively separated from neutrons using the RMS, while a cut on the rise-time allows to separate gamma signals (Fig. 4). However, given the shape variability of the alpha and neutron signals, it was not possible to unravel both contributions.

Therefore, applying the combination of the rise time and decay time, it is possible to discriminate micro-discharges and γ/β signals, to finally obtain a clean spectrum containing only neutron and alpha signals (Fig. 5).

From hereafter, we will show and refer to spectra on which these selections cuts have already been applied, unless stated otherwise.

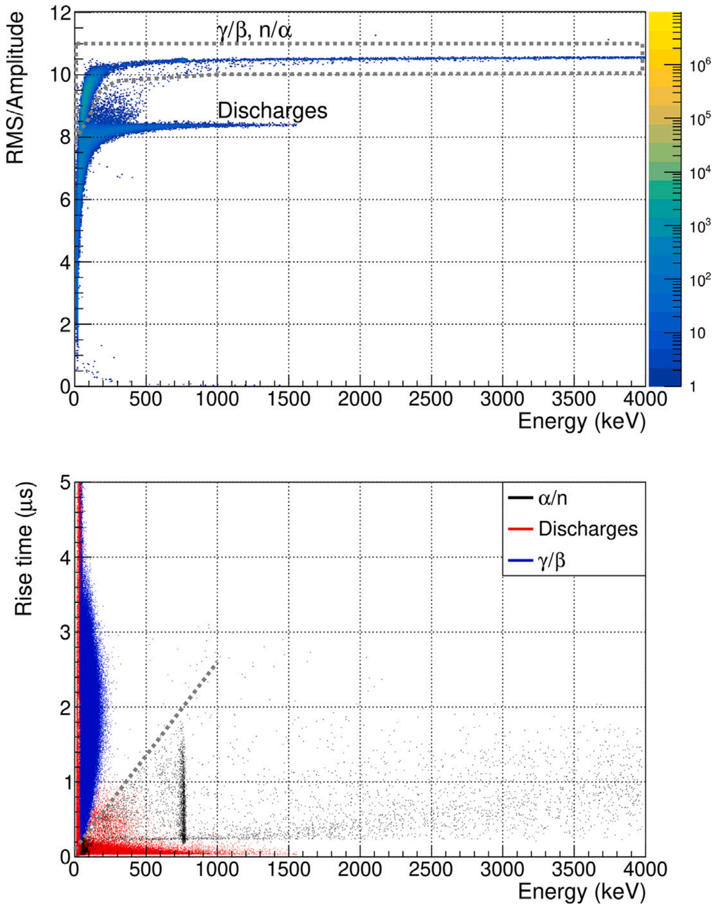

Fig. 4. Top: Normalized RMS versus deposited Energy scatter plot in the background measurement for one of the steel detectors. The dashed line shows the cut used to discard micro-discharge signals. Bottom: Rise time versus Energy discrimination plot showing each kind of signal. The dashed line shows the separation between γ/β and neutron/α signals.

3.2. *Neutron counts determination*

In the measured background spectra, there is a contribution of alpha events that has to be taken into account. The method followed for the determination of the neutron count rate from the clean spectrum, above mentioned, is based on a fitting procedure to a combination of a neutron and an alpha response.

From the calibration runs with ^{252}Cf, a neutron response function was obtained for each detector. For the alpha response, in the case of stainless steel detectors, the alpha count rate is low enough to observe the neutron total absorption peak at 764 keV, and also the wall effect down to 190 keV. Hence, the alpha contribution was approximated to an uniform distribution in the whole energy region (Fig. 6 bottom).

In the case of aluminium detectors, the alpha contribution is so high, that only the neutron total absorption peak can be seen. It also shows an structure that makes the use of an uniform distribution approach unfeasible. For this reason, the intrinsic alpha spectrum was measured inside a 40 cm thick polyethylene shield, and used as the alpha response function (Fig. 6 top).

Using these responses, the background spectra have been fitted to obtain the neutron counts for each detector. In the stainless steel detectors the spectrum region above 800 keV is fitted to the alpha uniform response and the region below this energy is then fitted to the combination of neutron and alpha responses. In the case of aluminum detectors, the alpha response is first normalized to the background measurement time. Then the spectrum is fitted to the neutron plus alpha responses.

4. Monte Carlo simulations

The isotropic and non-monochromatic neutron flux can be determined from the neutron count rate through Eq. (2):

$$R = \int S(E)\Phi(E)dE \tag{2}$$

where R is the neutron counting rate in s^{-1}, S(E) is the spectral neutron sensitivity of the detector in cm^2 and $\Phi(E)$ is the density neutron flux in $cm^{-2}s^{-1}$.

Typically, multiple-detector configurations, like Bonner sphere detectors [2,9,10], are used to determine experimentally both the integral value and the distribution of the neutron flux in several energy intervals and Eq. (2) becomes:

$$R^i = \sum_{j=1}^{N} S^i(E_j)\Phi(E_j) \tag{3}$$

where $S^i(E_j)$ is the calculated average sensitivity of the ith detector configuration, in the jth energy interval.

In our case, for the determination of the thermal neutron flux only two detector configurations have been used. The bare detector measurement has maximum sensitivity at thermal energies and decreases at higher energies. On the other hand, measurements with the detector wrapped in a 1 mm Cadmium shield are mostly sensitive to the epithermal region, due to the ^{113}Cd resonance in the cross section that absorbs neutrons below 0.32 eV. Thus, we have divided the energy spectrum into two ranges, from 10^{-4} to 0.32 eV for the thermal range and from 0.32 to 2.0×10^7 eV for the epithermal and fast neutron region.

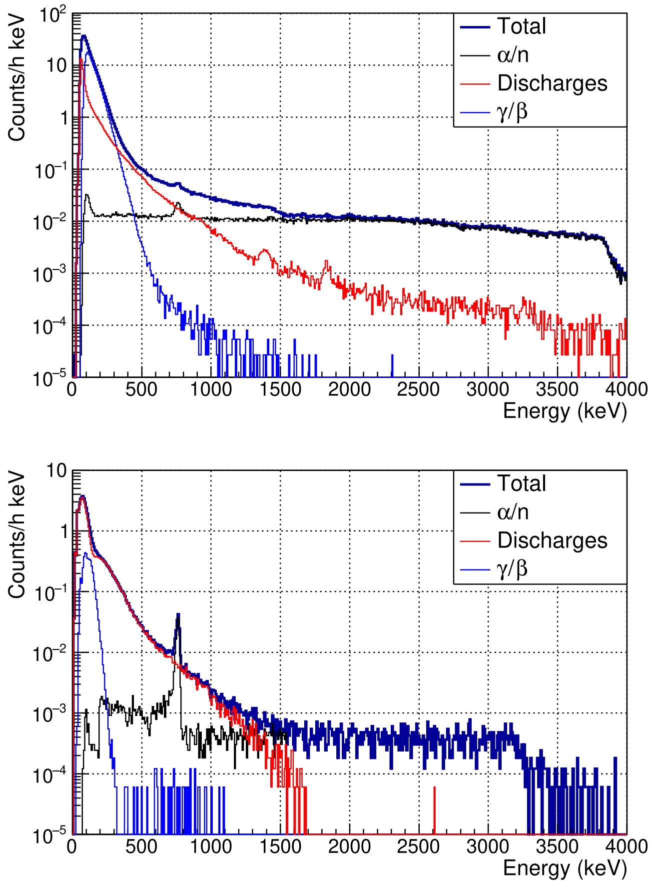

Fig. 5. Spectrum of partial accumulated measurement with different contributions discriminated. Top: Aluminum detector. Bottom: Stainless steel detector.

By applying Eq. (3), the measured count rates in both configurations can be separated into two contributions:

$$\begin{aligned} R^{bare} &= S_{th}^{bare}\Phi_{th} + S_{e+f}^{bare}\Phi_{e+f} \\ R^{Cd} &= S_{th}^{Cd}\Phi_{th} + S_{e+f}^{Cd}\Phi_{e+f} \end{aligned} \tag{4}$$

where R are the measured count rates in the detectors for the bare and Cd shielded configuration respectively, and S_{th}, S_{e+f} are the calculated neutron sensitivities in the thermal and epithermal+fast regions respectively.

The MCNP 6.2 [11,12] Monte Carlo (MC) particle transport code has been used to calculate the average neutron sensitivity of the ^{3}He detector configurations used in this experiment. The nuclear data library used was the ENDF/B-VII.1 version. The detectors have been simulated as simple cylinders with the dimensions and compositions listed in Table 1.

4.1. Code validation

Prior to the calculation of the neutron sensitivities, the code has been validated through the calculation of the detector response to the known neutron energy spectrum of ^{252}Cf. The simulation has been compared to the data measured during the calibrations runs. The ISO standard neutron spectrum for ^{252}Cf source [13] has been used. Special emphasis has been put on the description of the geometry of the ensemble source-moderator in order to minimize the uncertainties. Fig. 7 compares the experimental spectrum with the simulation response convoluted with a Gaussian function of 2.8% resolution at 764 keV.

Table 2
Comparison of simulated and experimental efficiency for the ^{252}Cf source.

Detector model	ϵ (%)	
	MCNPX	Experiment
25241 (Aluminum)	0.233 ± 0.001	0.22 ± 0.02
252266 (S Steel)	0.361 ± 0.001	0.32 ± 0.03

Table 3
Composition of the concrete used in the simulations.

Element	% mass	% atomic
H	0.5	9.3
O	51.1	59.7
Na	2.9	2.4
Al	3.4	2.4
Si	35.2	23.4
Ca	4.4	2.1
Fe	2.5	0.8
Density	2.15 g/cm^3	

Detection efficiency has been determined from the response spectra. Calculated values are given in Table 2 compared to the experimental values, showing an excellent agreement within an uncertainty of around 10%.

4.2. Thermal neutron sensitivity

The calculation of the average sensitivity for each energy range depends on the energy spectrum used for the calculation. A flux shape as realistic as possible should be used to obtain reliable values.

Jordan et al. [2] determined the energy distribution of the flux in Hall-A up to 100 MeV, but showed a large uncertainty in the thermal region and thus cannot be used to determine the sensitivity for that region.

Another approach is to determine a realistic flux through Monte Carlo codes (SOURCES4 A, SAG4N) [14–16]. Different processes such as natural fission or (α,n) reactions in the rocks act as the neutron source. These neutrons are then transported through the rocks themselves and the concrete layer surrounding the laboratory to yield a final flux spectrum inside the laboratory.

In the case of the LSC, the composition of the rock has been previously characterized [17]. However, the 40 cm thick layer of concrete covering the rock makes the neutron transport through the latter the dominant factor in the final neutron flux. But unfortunately, the composition of the concrete is unknown. Therefore, the effect of the concrete composition on the flux has been analyzed.

Several types of concrete with different composition and hydrogen contents were investigated [18]. They showed large differences in the ratios of thermal to higher neutron energy components (see Fig. 8 top). The shape of the flux can broadly be described as having two major components: a Maxwellian distribution on the thermal region, and an isolethargic distribution for higher energies. The differences between different concrete compositions can be described with different weights of both contributions.

Finally, an ordinary reinforced concrete with 9% of hydrogen content was used (Table 3), in accordance to other nuclear research facilities [19,20]. Therefore the neutron flux shape considered for our calculations is the resulting flux of a ^{238}U spontaneous fission neutron distribution, created in the rocks, and transported over a 40 cm thick layer of such concrete.

In order to account for the systematic uncertainty due to the concrete type used in the construction of the lab, both isolated shapes (maxwellian and isolethargic) were also considered in the calculations. The three neutron flux cases are shown in Fig. 8 bottom.

MCNP6.2 calculations have been performed in three different ways:

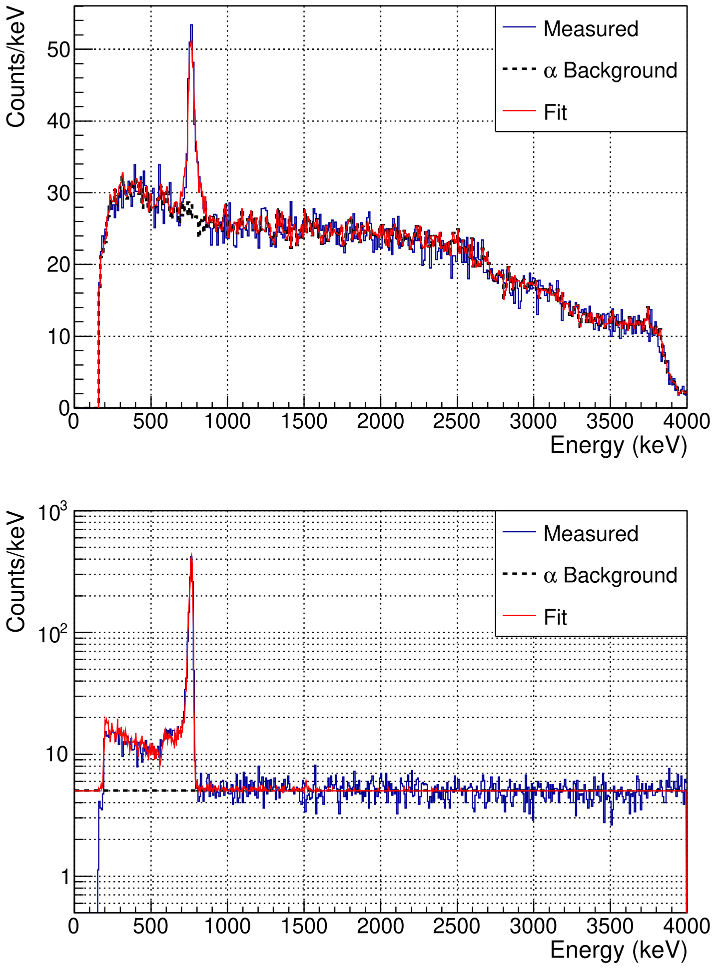

Fig. 6. Fit of neutron response to the experimental data from ^{3}He proportional counters. Top: Aluminum detector. Bottom: Stainless steel detector.

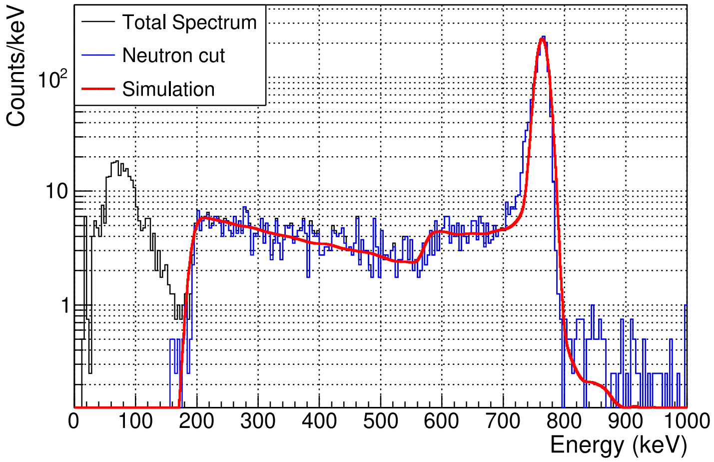

Fig. 7. Experimental Cf spectrum and MCNP simulation.

- Neutron flux tally (F4:n) convoluted with the ^{3}He(n,p)t reaction cross section by means of a tally multiplier (FM) card.
- Neutron pulse height tally (F8:n) with the FT8 CAP option, to turn it into a neutron capture tally.
- Neutron pulse height tally with the FT8 PHL (Pulse Height Light) option. This option allows combining the results of two energy deposition tallies (tally type 6), one for each charged reaction product (proton and triton), to obtain the energy deposited in coincidence within the detector [21]. For this calculation, MCNP's Neutron Capture Ion Algorithm (NCIA) is activated (card PHYS:N 6J 4). This method allows obtaining pulse height spectra, in addition to reaction rates.

The values obtained by all three methods are fully compatible within the statistical uncertainties. The F8:n FT8 CAP result was chosen as the reference value.

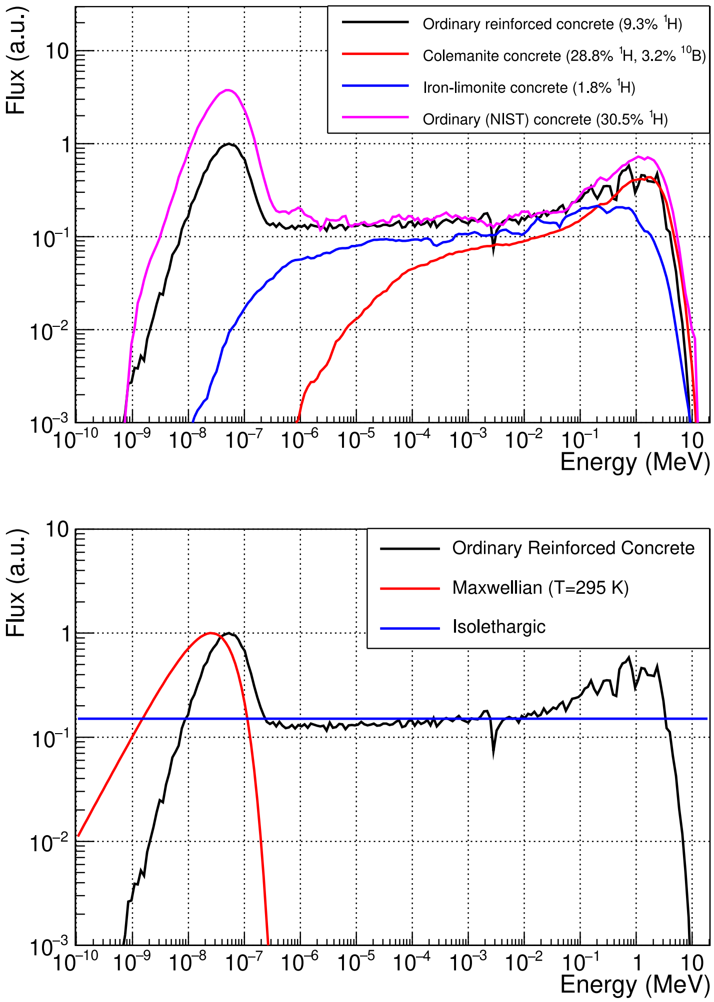

Fig. 8. Top: Flux spectra for spontaneous fission neutrons transported over different types of concrete. Bottom: Neutron fluxes considered in the calculations, using three different shapes: thermal Maxwellian distribution, isolethargic, and spontaneous fission transported over an ordinary reinforced concrete. Spectra are arbitrarily normalized only for comparison purposes.

Table 4
Average sensitivities for the thermal and epithermal+fast components corresponding to different shapes of the flux for bare and Cd shielded detectors.

25241 (Al cathode) (cm^2)					
	Maxwell	Isolethargic		Concrete	
	Bare	Bare	Cd	Bare	Cd
S_{th}	67.4 ± 1.3	75.8 ± 1.5	0.0	56.7 ± 1.1	0.0
S_{e+f}	0.0	4.0 ± 0.1	3.0 ± 0.1	3.0 ± 0.1	2.2 ± 0.1
252266 (SS cathode) (cm^2)					
	Maxwell	Isolethargic		Concrete	
	Bare	Bare	Cd	Bare	Cd
S_{th}	99.4 ± 5.0	95.0 ± 4.8	0.0	92.4 ± 4.6	0.0
S_{e+f}	0.0	9.6 ± 0.5	7.5 ± 0.4	7.1 ± 0.4	5.5 ± 0.3

Table 5
Statistics accumulated in each detector during the measurements.

Detector	Configuration	Period	Time (h)	n counts	Count Rate (h^{-1})
D1 (Al)	Bare	2019	3978	3805 ± 86	0.95 ± 0.02
D2 (Al)	Bare	2019	3978	3702 ± 106	0.93 ± 0.03
D1 (Al)	Bare	2020	2333	1832 ± 75	0.78 ± 0.03
D2 (Al)	Bare	2020	4661	3579 ± 159	0.77 ± 0.03
D3 (SS)	Bare	2020	2062	2643 ± 56	1.28 ± 0.03
D4 (SS)	Bare	2020	9080	11915 ± 135	1.31 ± 0.01
D1 (Al)	Polyethylene	2020	5256	–	–
D2 (Al)	Cadmium	2020	2062	43 ± 43	0.02 ± 0.02
D3 (SS)	Cadmium	2020	3194	501 ± 27	0.157 ± 0.008

Table 4 shows the computed sensitivities for each detector configuration, energy range and flux shape. Taking into consideration systematic uncertainties in the geometry(detector parameters) such as gas pressure, or detector dimensions, a conservative uncertainty of 2% was applied to aluminum detector values, and 5% to stainless steel ones.

5. Results and discussion

Background measurements were grouped in two periods of time. For the first campaign in 2019, only the aluminium detectors were available in the bare configuration. For the second campaign, during 2020 and 2021, the two stainless steel detectors were added to the setup. One aluminum detector was put inside the polyethylene shield, while the Cadmium shield was used alternatively between the other aluminium detector and one of the stainless steel detectors.

Detector data for each campaign and configuration were analyzed according to the procedure described in Section 3. The resulting average neutron count rates are summarized in Table 5.

A difference of about 20% in the count rate for the aluminum detectors was observed between the two campaigns (D1 and D2 detectors in Table 5).

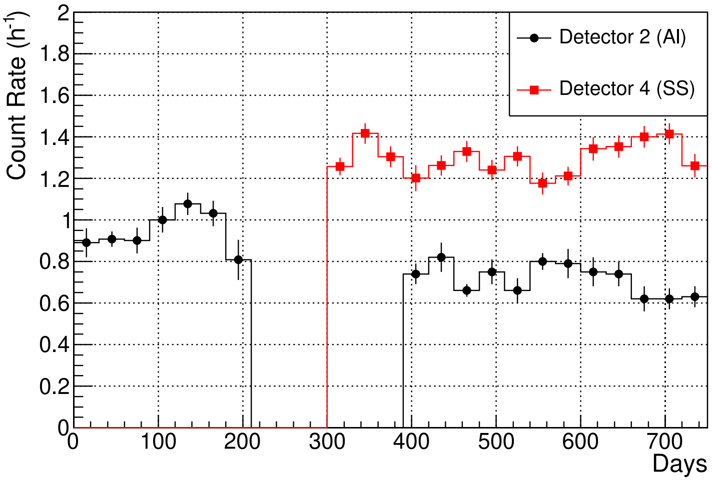

Fig. 9. Stability of neutron count rate in 30-day periods.

Table 6
Thermal flux calculated for each detector and simulated flux shape.

Detector	Period	Φ_{th}($\times10^{-6}$n/cm^{2}s)		
		Maxwell	Isolethargic	Concrete
D1 (Al)	2019	3.9 ± 0.1	3.4 ± 0.2	4.5 ± 0.2
D2 (Al)	2019	3.8 ± 0.1	3.3 ± 0.2	4.4 ± 0.2
D1 (Al)	2020	3.2 ± 0.2	2.8 ± 0.2	3.7 ± 0.3
D2 (Al)	2020	3.2 ± 0.2	2.7 ± 0.2	3.6 ± 0.2
D3 (SS)	2020	3.6 ± 0.2	3.2 ± 0.2	3.3 ± 0.2
D4 (SS)	2020	3.7 ± 0.2	3.2 ± 0.2	3.3 ± 0.2
	Average	3.5 ± 0.8		

The reason for the change in the neutron count rate is uncertain at the moment. Environmental variables like radon concentration and moisture are regularly measured at some points of LSC's Hall A, but no apparent correlations were found. On the other hand, modifications in the setup of the surrounding experiments during the four-month interval between the end of the 2019 period and the start of the 2020/2021 period is a plausible cause for the change.

The accumulated 30-day neutron rate was calculated in order to assess the stability of the count rate. Fig. 9 shows the count rates for detector D2 (aluminum) and D4 (stainless steel) in 30-day periods. It can be seen that, except for the change between both campaigns for the aluminum detector, the rates remain within statistical fluctuations for both detectors during the two measurement periods.

Using the count rates obtained for the different configurations and the calculated sensitivities, the thermal flux has been calculated for the three flux shapes assumed in Section 4.2 by solving Eq. (4). Table 6 summarizes the calculation of the thermal flux with the detectors available in each period.

It should be noted that we used two types of detectors with very different ^{3}He pressure. This difference becomes evident when looking at the calculated sensitivities. Despite the differences in shape of the simulated fluxes and the detectors, calculated values agree within a 20% of uncertainty. The average of all values has been calculated for the thermal neutron flux in Hall-A: Φ_{th} = (3.5±0.8)×10^{-6} n/cm^{2}s. The final value includes statistical and systematic uncertainties.

In a previous measurement, Jordan et al. obtained a thermal neutron flux between 2 × 10^{-8} and 2.2 × 10^{-6} n/cm^{2}s depending on the deconvolution method used. Their setup was not sensitive enough to the thermal range, and hence the high uncertainty. Our measurement was specifically aimed to determine this value, which makes it more reliable. Even so, the larger of Jordan et al. values is comparable to ours.

Table 7
Thermal neutron flux in other facilities and this work.

Location	m.w.e	Thermal flux ($\times10^{-6}$n/cm^{2}s)
LSM [22]	4800	1.6(1)
LNGS (Hall C) [23–25]	3800	0.54–2.05
SURF [4]	4300	1.7–9.9
LNGS (Hall-A) [4]	3800	0.32(9)
Soudan [4]	2090	0.70(8)
WIPP [4]	2000	<0.06
KURF [4]	1450	< 0.4
Slanic [26]	600	0.12(4)
Kamioka [27,28]	2700	8.26–7.88
CJPL-I [29]	6720	7.03(1.81)
Yangyang (A5-A6) [30,31]	2000	14.4(1.5)–24.2(1.8)
SNOlab [32,33]	6000	4.79 (0.13)
LSC Hall-A [2,3]	2450	0.02 to 2.2
LSC Hall-A (this work)	2450	3.5(8)

5.1. *Comparison to other underground facilities*

We have compared our value for the thermal neutron flux in LSC Hall-A with other underground facilities around the world, measured with similar setups. Table 7 summarizes the values of the thermal flux obtained in those facilities.

The value obtained in this study is comparable to measurements performed at LSM [22] and SURF [4]. Older values measured in Hall-C at LNGS are also in the same order of magnitude [23–25], and more recent values in Hall-A at LNGS are one order of magnitude lower [4]. A recent measurement at Slanic Prahova Salt Mine also shows a thermal flux one order of magnitude lower [26]. LSC thermal neutron flux is within an order of magnitude of other similar laboratories.

6. Conclusions

A direct measurement of the thermal neutron background has been performed for the first time at Hall-A of Laboratorio Subterráneo of Canfranc. Two types of high efficiency ^{3}He detectors were used in bare and Cd wrapped configurations to carry out the measurements.

Low rate measurements can be greatly affected by intrinsic contamination sources like alpha decays in the cathode, or electric noise like microdischarges. A dedicated pulse shape analysis was developed that allowed us to discriminate neutrons from gamma and microdischarge events, and improve the neutron count rate estimation.

Neutron sensitivities for each type of detector have been calculated by means of Monte Carlo techniques, and using different flux shapes to estimate the systematic uncertainty. Despite the differences in the detectors characteristics, and the simulated flux shapes, the final calculation of the thermal flux values agreed within a 20% of uncertainty.

An average value of Φ_{th}= 3.5±0.8×10^{-6} n/cm^{2}s has been determined for the thermal flux in Hall-A of LSC. The value is within an order of magnitude compared to other similar facilities.

Declaration of competing interest

The authors declare that they have no known competing financial interests or personal relationships that could have appeared to influence the work reported in this paper.

Data availability

Data will be made available on request.

Acknowledgments

This work was supported partially by the Spanish Ministerio de Ciencia e Innovación and its Plan Nacional de I+D+i de Física de Partículas projects: FPA2016-76765-P and FPA2018-096717-B-C21. The authors want to acknowledge the help provided by the staff at LSC in the preparation and support for this work.

References

[1] J.M. Carmona, et al., Astropart. Phys. 21 (2004) 523.
[2] D. Jordan, et al., Astropart. Phys. 42 (2013) 1.
[3] D. Jordan, et al., Corrigendum to 'measurement of neutron background at the canfranc underground laboratory LSC', Astropart. Phys. 42 (2013) 1.
[4] A. Best, et al., Nucl. Inst. and Meth. A 812 (2016) 1.
[5] LND Inc. (http://www.lndinc.com/).
[6] Teledyne SP Devices (https://www.spdevices.com/).
[7] K.M. Heeger, et al., IEEE Trans. Nucl. Sci. 47 (2000) 1829–1833.
[8] T.J. Langford, et al., Nucl. Inst. Meth. A 717 (2013) 51.
[9] R.L. Bramblett, R.I. Ewing, T.W. Bonner, Nucl. Instr. Meth. 9 (1960) 1.
[10] M. Grieger, et al., Phys. Rev. D 101 (2020) 123027.
[11] C.J. Werner, et al., MCNP User's Manual, Los Alamos National Laboratory report LA-UR-17-29981, 2017.
[12] C.J. Werner, et al., MCNP Version 6.2 Release Note, Laboratory report LA-UR-18-20808, 2018.
[13] Reference neutron radiations. Part I - Characteristics and methods of production. ISO8529-1:2001.
[14] W.B. Wilson, et al., SOURCES4A: A Code for Calculating (α, n), Spontaneous Fission, and Delayed Neutron Sources and Spectra, Technical Report LA-13639-MS, Los Alamos, 1999.
[15] E. Mendoza, et al., Nucl. Inst. Meth. A 960 (2020) 163659.
[16] V. Tomasello, et al., Nucl. Inst. Meth. A 595 (2008) 431.
[17] J. Amaré, et al., J. Phys.: Conf Ser. 39 (2006) 151.
[18] R.J. McConn Jr., et al., Compendium of Material Composition Data for Radiation Transport Modeling, Pacific Northwest National laboratory Report, PNNL-15870 Rev1, 2011.
[19] R. Méndez-Villafañe, et al., Radiation Protection Dosimetry, Vol. 161, no. 1–4, 2014, pp. 393–397.
[20] K.A. Guzmán-García, R. Méndez-Villafañe, H.R. Vega-Carrillo, Appl. Radiat. Isot. 100 (2015) 84–90.
[21] M.T. Swinhoe, J.S. Hendricks, Calculation of the Performance of 3He Alternative Detectors with MCNPX, Los Alamos National Laboratory report LA-UR-11-03050, 2011.
[22] V. Chazal, et al., Astropart. Phys. 9 (1998) 163.
[23] A. Rindi, F. Celani, M. Lindozzi, S. Miozzi, Nucl. Inst. Meth. A 272 (1988) 871.
[24] P. Belli, et al., Nuovo Cimento A 101 (1989) 959.
[25] Z. Debicki, et al., Nucl. Phys B - Proc. Suppl. 196 (2009) 429.
[26] Z. Debicki, et al., Nucl. Inst. Meth. A 910 (2018) 133.
[27] A. Minamino, (Master Thesis), The University of Tokyo, 2004, (http://www-sk.icrr.u-tokyo.ac.jp/xmass/publist/master-minamino.pdf).
[28] K. Mizukoshi, et al., Prog. Theor. Exp. Phys. 2018 (2018) 000.
[29] Q. Hu, et al., Nucl. Inst. Meth. A 859 (2017) 123C01.
[30] H. Park, et al., App. Radiat. Isot. Astropart. Phys. 81 (2013) 302.
[31] Y.S. Yoon, et al., Astropart. Phys. 126 (2021) 102533.
[32] M.C. Browne, (Ph.D. thesis), North Carolina State University, 1999.
[33] M. Barnabé-Heider, et al., Phys. Lett. B 624 (2005) 186.